Spatiotemporal reaction kinetics of an ultrafast photoreaction pathway visualized by time-resolved liquid x-ray diffraction

Tae Kyu Kim[†], Maciej Lorenc[‡§], Jae Hyuk Lee[†], Manuela Lo Russo[‡], Joonghan Kim[†], Marco Cammarata[‡¶], Qingyu Kong[‡], Sylvie Noel[‡], Anton Plech[‖], Michael Wulff[‡††], and Hyotcherl Ihee[†‡‡]

[†]Department of Chemistry and School of Molecular Science (BK21), Korea Advanced Institute of Science and Technology (KAIST), Daejeon 305-701, South Korea; [‡]European Synchrotron Radiation Facility, Grenoble Cedex 9, France; [¶]National Institute for the Physics of Matter and Department of Physical and Astronomical Sciences, University of Palermo, via Archirafi 36, 90123 Palermo, Italy; and [‖]Fachbereich Physik der Universität Konstanz, Universitätsstrasse 10, D-78457 Konstanz, Germany

Edited by Peter M. Rentzepis, University of California, Irvine, CA, and approved May 9, 2006 (received for review March 10, 2006)

We have studied the reaction dynamics for HgI_2 in methanol by using time-resolved x-ray diffraction (TRXD). Although numerous time-resolved spectroscopic studies have provided ample information about the early dynamics of HgI_2, a comprehensive reaction mechanism in the solution phase spanning from picoseconds up to microseconds has been lacking. Here we show that TRXD can provide this information directly and quantitatively. Picosecond optical pulses triggered the dissociation of HgI_2, and 100-ps-long x-ray pulses from a synchrotron probed the evolving structures over a wide temporal range. To theoretically explain the diffracted intensities, the structural signal from the solute, the local structure around the solute, and the hydrodynamics of bulk solvents were considered in the analysis. The results in this work demonstrate that the determination of transient states in solution is strongly correlated with solvent energetics, and TRXD can be used as an ultrafast calorimeter. It also is shown that a manifold of structural channels can be resolved at the same time if the measurements are accurate enough and that global analysis is applied. The rate coefficients for the reactions were obtained by fitting our model against the experimental data in one global fit including all *q*-values and time delays. The comparison between all putative reaction channels confirms that two-body dissociation is the dominant dissociation pathway. After this primary bond breakage, two parallel channels proceed. Transient HgI associates nongeminately with an iodine atom to form HgI_2, and I_2 is formed by nongeminate association of two iodine atoms.

HgI_2 | hydrodynamics | liquid phase | molecular structural dynamics | transient structure

The knowledge of temporally varying molecular structures during ultrafast processes is vital in understanding the mechanism and function of molecular reaction. During the last decades, the dynamics of molecular reactions have been investigated by numerous spectroscopic techniques with femtosecond time resolution. However, the direct determination, at atomic resolution, of the structural dynamics involved in such processes can only be obtained by time-resolved x-ray (1–5), electron diffraction (6–9) and x-ray absorption spectroscopy (10, 11) acting as atomic probes. The methodology of time-resolved x-ray/electron diffraction is similar to ultrafast optical pump–probe experiment: a femtosecond laser pulse triggers a reaction in the molecules, and a delayed electron or x-ray pulse, rather than an optical pulse as in optical spectroscopy, probes the structural evolution. The changes in the nuclear coordinates are directly recorded by varying the time delay between the laser and the x-ray/electron pulse.

Because the scattering cross section of hard x-rays is 6 orders of magnitude lower than for electrons (12, 13), time-resolved x-ray diffraction (TRXD) can penetrate condensed samples such as liquids. In the condensed phase, the dynamics are not only determined by the potential energy surfaces of the reactant-product species, but the surrounding solvent also plays a crucial role in modifying the energies of all species and imposing the reaction pathway (14). Because the diffraction method is sensitive to all species in the solution, the changes in scattering due to photoexcitation fall in several classes of diffraction modifications: (*i*) the structural changes in the solutes by the photoreaction, (*ii*) the changes of cage structure, and (*iii*) the solvent's structural change due to the energy transfer [such as heating and thermal expansion (1, 15–18)]. By calculating these three contributions using molecular dynamics (MD) simulations, the complex structural dynamics of photo-excited $C_2H_4I_2$ in methanol was recently elucidated (1). In our continuing effort to develop TRXD, we report here the determination of the reaction pathway and structural dynamics spanning a time window from 100 ps to 1 μs after the photodissociation of HgI_2 in methanol. The unprecedented precision in the evaluation of transient-state concentrations and the energy transduction pathway allows one to determine the signature of subtle structural reorganization of solvation cage. In our approach, the solvent differentials for methanol (16) due to density and temperature changes were quantified separately by using near-IR laser pulse, and they were used in this work. This approach provides excellent agreement between experimental and theoretical diffraction curves.

Several femtosecond-resolved spectroscopic studies of the dissociation of HgI_2 in the gas phase have been performed (19–21). Zewail and coworkers (20) focused on the two-body reaction ($HgI_2 \rightarrow HgI + I$) by monitoring HgI formation up to 3 ps using laser-induced fluorescence. On the other hand, both two- and three-body dissociations ($HgI_2 \rightarrow Hg + I + I$) were observed and studied by using time-resolved mass spectrometry (21). In the solution phase, Hochstrasser and coworkers (22–24) investigated the solvation dynamics of HgI_2 dissolved in ethanol at delays up to 15 ps by using femtosecond absorption spectroscopy and discussed in detail the vibrational relaxation process and rotational dynamics of HgI molecules generated through

Conflict of interest statement: No conflicts declared.

This paper was submitted directly (Track II) to the PNAS office.

Freely available online through the PNAS open access option.

Abbreviations: TRXD, time-resolved x-ray diffraction; RDF, radial distribution function; MD, molecular dynamics.

[§]Present address: Groupe Matiere Condensee et Materiaux UMR6626, Centre National de la Recherche Scientifique, BAT11A Campus de Beaulieu, Universite de Rennes 1, 35042 Rennes Cedex, France.

[††]To whom correspondence may be addressed at: European Synchrotron Radiation Facility 6, Rue Jules Horowitz BP 220, Grenoble Cedex 38043, France. E-mail: wulff@esrf.fr.

[‡‡]To whom correspondence may be addressed at: Department of Chemistry, Korea Advanced Institute of Science and Technology (KAIST), 373-1 Guseong-dong, Yuseong-gu, Daejeon, 305-701, South Korea. E-mail: hyotcherl.ihee@kaist.ac.kr.

© 2006 by The National Academy of Sciences of the USA

www.pnas.org/cgi/doi/10.1073/pnas.0601958103

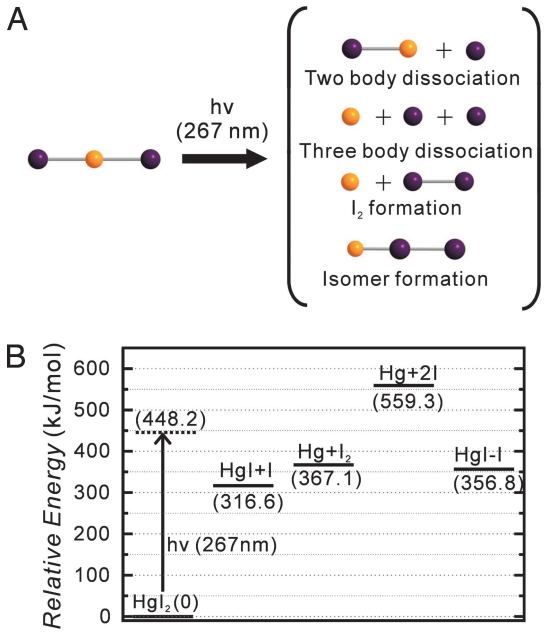

Fig. 1. Schematic diagram for reaction channels and energies in photodissociation of HgI_2 in solution. (*A*) Putative reaction channels after photodissociation of HgI_2 in solution. (*B*) Relative energies of the dissociation products of HgI_2 in solution. All values were calculated by density functional theory.

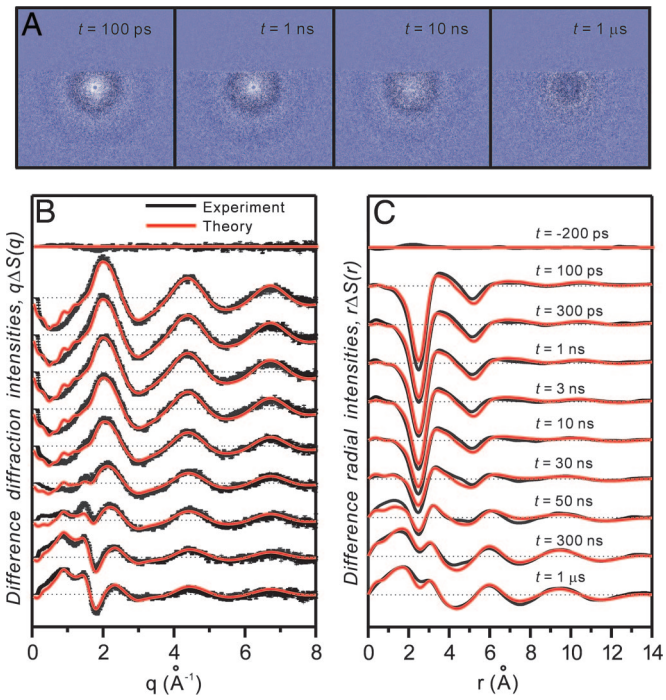

Fig. 2. TRXD signal as a function of time delay for HgI_2 in methanol. (*A*) Raw difference images on the detector for selected time delays. (*B*) Difference–diffraction intensities, $q\Delta S(q)$, excited minus nonexcited. Shown are radial averages of the 2D images from *A*. Error bars represent the experimental error associated with each scattering angle. (*C*) Difference RDFs, $r\Delta S(r)$. Shown are sine-Fourier transforms of the difference intensities in *B*.

impulsive photodissociation. However, a comprehensive reaction mechanism in the solution phase spanning from picoseconds up to microseconds has been lacking, and TRXD can now provide this information directly. Upon UV excitation, HgI_2 in solution can dissociate in four ways (Fig. 1): (*i*) a new transient species HgI plus an I atom, (*ii*) Hg + I + I, (*iii*) Hg + I_2, and (*iv*) an HgI–I isomer. Fig. 1 displays the schematics and reaction energies of these reaction channels. This molecular system was previously investigated by using TRXD, but because of the poor signal-to-noise ratio and limited data analysis, the transient reaction pathway could not be clearly unraveled (25). Because the difference diffraction curve of each reaction channel is similar in the high q region, solvent contributions due to the energy transfer from excited solute molecules should be included in the analysis to discriminate the primary reaction channel. Here we determined the primary reaction pathway and subsequent structural dynamics of dissociated HgI_2 in methanol by analyzing the data globally (1). The results presented in this work demonstrate that determination of transients in solution is strongly correlated with solvent energetics and that TRXD is, in addition to being a very sensitive structural probe, an ultrafast calorimeter. We also show that a manifold of structural channels can be resolved at the same time if only the measurements are sufficiently accurate and if global analysis is applied.

Results and Discussion

General Information from Difference–Diffraction and Radial Curves. To resolve the structural changes during the course of photodissociation, diffraction data were collected for 10 time delays from −200 ps up to 1 μs, and each delay was interleaved by a measurement at −3 ns, which served as reference for the unperturbed sample. Because the diffracted intensities from the structural changes are much smaller than total intensities, the difference intensities caused by the photoexcitation needs to be extracted carefully, a prerequisite for the analysis of structural relaxations (1, 15–18) (see also Figs. 6 and 7, which are published as supporting information on the PNAS web site, for details and control experiments).

As seen in Fig. 2 *B* and *C*, there is no difference intensity at −200 ps, which confirms the accurate timing between the laser and x-ray pulses. At positive time delays, the difference features appear and progress with the time. Because the high-Z Hg and I atoms in the solute scatter the x-rays more strongly than the low-Z atoms in methanol, the structural changes in the solutes stand out in the radial distribution functions (RDFs). Therefore, an intuitive interpretation of the structural changes in the solutes can be obtained from the RDF. The RDFs in Fig. 2*C* exhibit both negative and positive peaks: there are strong depletions of correlation at 2.65 and 5.30 Å with a corresponding rise at 3.50 Å at early times. Because the structural parameters of HgI_2 are well known and also confirmed by our calculations (Table 1), one can easily assign the two negative peaks to the bond breakage of Hg–I in HgI_2. More specifically, 5.30 Å corresponds to the depletion of I···I internuclear pairs in HgI_2, and 2.65 Å corresponds to the depletion and formation of Hg–I pair. The detailed analysis must include all three contributions: solute–solute,

Table 1. Summary of structural parameters and energies for various molecular species from the density functional theory calculations

Channel	Hg–I, Å	I–I, Å	I–Hg–I, °	Hg–I–I, °	Relative energy, kJ/mol
HgI_2	2.649	5.298	180.00	—	0.0
HgI–I	2.752	2.974	—	179.62	356.8
HgI	3.064	—	—	—	—
HgI + I	—	—	—	—	316.6
Hg + I_2	—	—	—	—	367.1
Hg + 2I	—	—	—	—	559.3

solute–solvent, and solvent–solvent (1, 17), which are described in the following section.

Global Fitting Analysis of Difference–Diffraction Curves. To fit the measured $\Delta S(q, t)$ [$q = (4\pi/\lambda)\sin(2\theta/2)$, where λ is the wavelength of the x-rays, θ is the scattering angle, and t is the time delay] curves for all time delays, the total theoretical intensities were calculated by considering the three principal contributions to the signal. Theoretical diffraction curves, which include the structural changes of solutes and cages, were generated by MD simulations for the putative reaction pathways described above. The structural change in the solute–solvent cages is due to changes in interatomic distances between solute–solvent pairs. The pure solvent contribution originates from heating and subsequent thermal expansion. This heating is induced by the transfer of energy from the photon-absorbing solutes to the surrounding solvent. The underlying general mechanism is that vibrational relaxation of a nascent molecule is very fast, typically over in 10–100 ps, which causes the temperature of the solvent to rise locally on that time scale. The time scale for expansion relaxation, in contrast, is linked to the release of the pressure gradient in the laser spot, which generates a density wave that travels outwards at the speed of sound. The overpressure is typically released in 50 ns for our sample dimensions.

The adiabatic expansion reestablishes the ambient pressure in ≈50 ns (18). Recently, we showed that these hydrodynamic effects, i.e., the solvent response to an ultrafast temperature rise, can be determined experimentally in pure methanol, without inducing any chemical change, by exciting it with near-IR laser pulses that excite overtones in C–H and O–H vibrations (16).

In the following, the global fitting of the diffraction curves to the theoretical model will be described. The basis set of model functions consists of the solvent terms $\{(\partial S(q, t)/\partial T)_\rho$ and $(\partial S(q, t)/\partial \rho)_T\}$, the difference scattering functions from transitions in the solutes alone, and their caged equivalents. If we consider two-body dissociation, we have three possible species and photoproducts (HgI_2, HgI, and I) that were MD-simulated in methanol. From the MD pair correlation functions $g_{\alpha\beta}(r)$ for atom pairs α and β, the solution scattering is derived from

$$S(q) = \sum_{\alpha\beta} f_\alpha(q) f_\beta(q) \cdot \left(N_\alpha \delta_{\alpha\beta} + \frac{N_\alpha N_\beta}{V} \int_0^\infty (g_{\alpha\beta}(r) - 1) \frac{\sin(qr)}{qr} 4\pi r^2 dr \right), \quad [1]$$

where $f_\alpha(q)$ is the atomic formfactor of the α atom, N_α is the number of α atoms in the MD simulation, and V is the volume of the MD box. After having calculated all putative structural transitions, the experimental difference curves at each time delay were fit to a linear combination of all putative components constrained to energy conservation within the x-ray illuminated volume. It should be noted that the multiplicative parameters for the components are not simple floating parameters, but they are mathematically linked by energy and mass conservation and hydrodynamics (e.g., the transformation of an HgI_2 molecule into the HgI radical and an iodine atom requires that from the initial 448.2 kJ/mol photon, 131.6 kJ/mol is dissipated into the solvent, whereas 316.6 kJ/mol amounts for the potential energy of the products; after recombination this energy will also be dissipated). From the simulation of the time-dependent solute concentrations, which release energy into the solvent, the time-dependent temperature and density changes of the solvent are obtained (15). The strategy of the least-squares fits to the experimental data with the set of the model functions is to minimize the total χ^2 iteratively in a global-fitting procedure

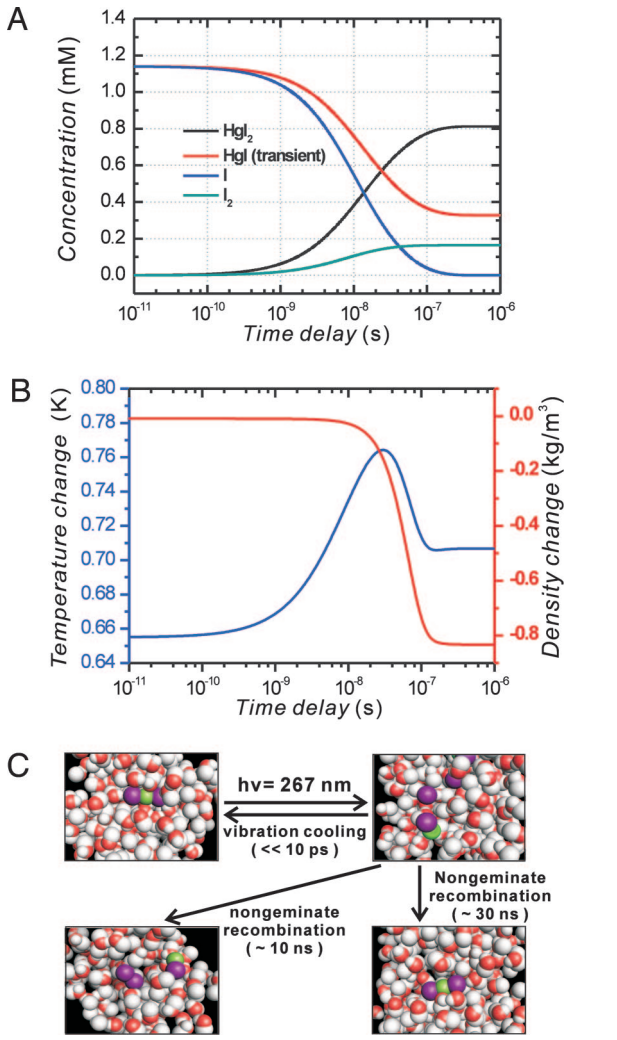

Fig. 3. Spatiotemporal reaction kinetics determined by TRXD. (*A*) The population changes of the various molecular species as a function of time delay after photodissociation of HgI_2 in methanol. (*B*) The change in the solvent density (red) and temperature (blue), where the baseline stems from the geminate ultrafast reaction pathway. Note the duality between the decay in excited-state population and the rise in temperature. (*C*) A schematic reaction mechanism determined by TRXD in solution.

(simultaneously minimizing the curves at all positive time delays) by using a home-made algorithm

$$\chi^2 = \sum_{j=\text{time delay}} \chi_j^2 \quad \text{and} \quad [2]$$

$$\chi_j^2 = \sum_i \left(\frac{\Delta S_{\text{theory}}(q_i, t_j) - \Delta S_{\text{experimental}}(q_i, t_j)}{\sigma_{i,j}} \right)^2,$$

where $\sigma_{i,j}$ is the error bar on the experimental curves calculated as the standard deviation of the different repetitions of a given time delay. The fitting parameters are the rate constants for dissociation, $HgI_2 \rightarrow HgI + I$, geminate and nongeminate recombination $HgI + I \rightarrow HgI_2$, and the nongeminate formation of molecular iodine $I + I \rightarrow I_2$. Furthermore, the occupancies of the respective species enter the fitting under the restriction that the number of atoms is conserved. The last fitting parameter is the laser beam size, which is used to optimize the time constant

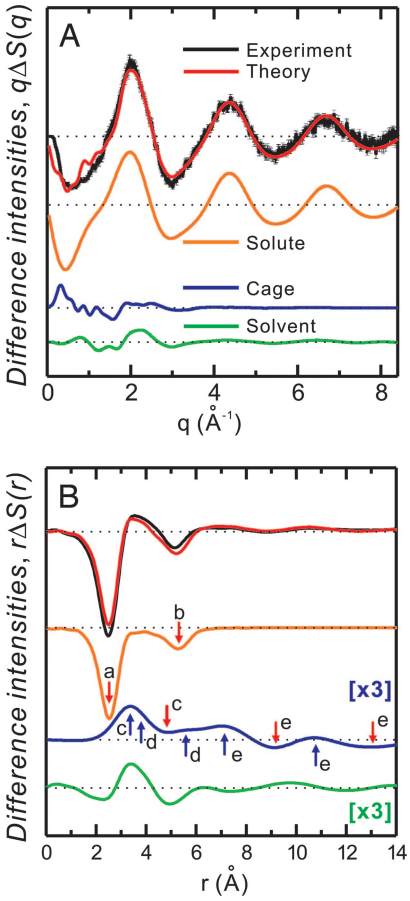

Fig. 4. Contributions from the solute-only, solute–solvent (cage), and solvent–solvent correlations to the difference intensities and the difference RDFs for HgI_2 in methanol. The curve fitting is based on MD and experimental solvent differentials and includes intramolecular and intermolecular contributions from the solutes and the solvent. The experimental (black, with experimental errors) and theoretical (red) difference intensity (*A*) and difference RDFs (*B*) at 100 ps are shown. Also shown are the decomposed components: solute without cage (orange), cage effects (blue), and solvent contribution (green). Decomposed components of cage effects (blue) and solvent contribution (green) in *B* are multiplied by a factor of 3 to magnify major peaks and valleys. The assignments of the main components for the major peaks and valleys in *B* are given as follows: (a) Hg–I of HgI_2 and HgI; (b) I···I of HgI_2; (c) Hg···solvent; (d) I···solvent; and (e) I···solvent and Hg···solvent. The assignments for the solvent-only term (the last curve) are not shown here but were given in one of our previous publications (1).

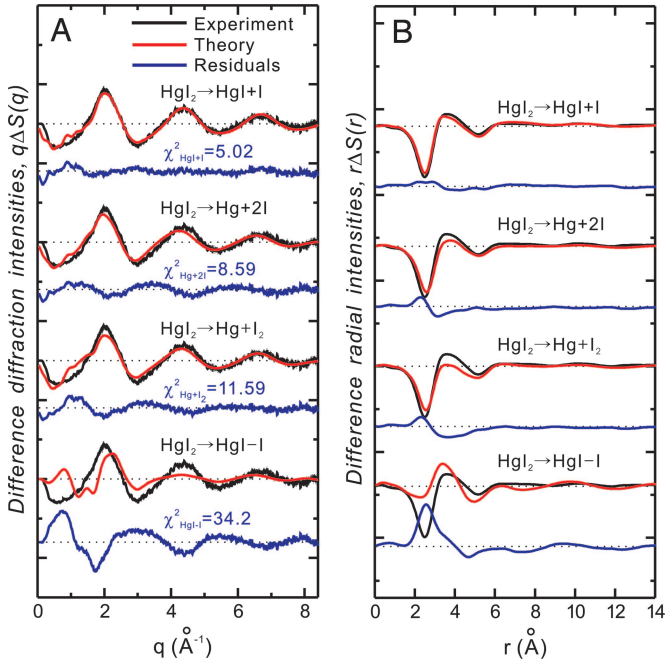

Fig. 5. Determination of the photodissociation pathway of HgI_2 in methanol. Theoretical (red) and experimental (black) difference intensities for candidate channels are shown in $q\Delta S(q)$ curves (*A*) and $r\Delta S(r)$ curves (*B*). The differences (residues) between theoretical and experimental curves are also shown in blue. χ^2 values for each channel from the global-fitting at 100 ps are shown. The channel $HgI_2 \rightarrow HgI + I$ gives the best fit.

of thermal expansion. Optimal fits to all experimental data using a kinetic model for $HgI_2 \rightarrow HgI + I$ and following several reactions are shown in Fig. 2 *B* and *C*. The fitted theoretical curves successfully reproduce experimental difference curves. The global-fitting process provides, as a function of time, chemical population changes and the temperature and density change of the solvent (Fig. 3 *A* and *B*).

Structural Dynamics and Energy Dissipation. Fig. 3*A* shows the population changes of all related chemical species from the global fitting. HgI and I are the dominant species at 100 ps, and they originate from two-body dissociation, which is essentially completed within a few picoseconds (26, 27). Then 71 ± 1.2% of the transient HgI radicals recombine nongeminately with iodine atoms that have escaped from another solvent cages to form the parent molecule HgI_2. A bimolecular rate constant of 1.0 (±0.1) × 10^{11} $M^{-1}{\cdot}s^{-1}$ for the nongeminate formation of HgI_2 was determined. On the other hand, 29 ± 0.5% of all iodine atoms combine to form I_2 with the rate constant 3.3 (±0.5) × 10^{10} $M^{-1}{\cdot}s^{-1}$. The time constant for the nongeminate recombination of I_2 is close to the values found in CCl_4 solutions from optical spectroscopy (28). HgI_2 forms faster than I_2, implying that the activation energy for the formation of HgI_2 is lower than that for I_2.

After thermal expansion, the density of the solvent decreased by 0.83 kg/m^3 at 1 μs, which corresponds to the temperature change of 0.71 K. Considering the final concentrations of all solute species (HgI_2, HgI, and I_2) and the reaction energies in the chemical reactions, we predict a temperature rise of 0.22 K rather than the observed 0.71 K. This deficiency of transiently observed species reveals an important contribution from fast geminate recombination of initially excited molecules, which is not visible with the current 100-ps time resolution. As a consequence, it is estimated that 66 ± 3.8% of initial HgI_2^* molecules decay into the ground state (in cage vibrational cooling) and release their energy to the solvent by means of collisions on the 10-ps time scale (29), whereas the remaining 34 ± 3.8% dissociates into HgI + I. In the 10 mM concentration of HgI_2 in methanol, we find that 33 ± 3.1% of the molecules are excited by the laser pulse.

Decomposition of the Data into Structural Elements. In the global-fit analysis, the data are decomposed into the change due to the solvent only, the change in the solvation cage, and the hydrodynamics response of the solvent. In Fig. 4, the decomposition into these contributions for 100-ps time delay is shown as $q\Delta S(q)$ and $r\Delta S(r)$ curves. Because of the heavy Hg and I atoms in the solute, the solute dynamics dominates over those from the cage and the solvent. However, the contributions from the cage and the solvent are significant in the low q region. The $r\Delta S(r)$ gives a more direct structural picture. The negative peaks at ≈2.65 Å are mainly due to the change in solute structure from the depletion of the Hg–I bond in HgI_2 and formation of new Hg–I bond in the transient. The second negative peak near 5.30 Å is due

to the I···I distance in the parent molecules. The positive peak at ≈3.50 Å can only be explained by changes in the cages and the solvent. A comprehensive explanation can be given by noting that the bond breaking in HgI_2 only induces negative signals in the change in pair correlation, while at the same time, the solvent molecules get closer to the solutes, which explains the positive signal in the cage correlation. The observed correlations in the bulk solvent can be interpreted as being due to the isochoric heating, which leads to the spreading of methanol–methanol distance distribution.

Determination of the Primary Reaction Pathway. To consider the various photodissociation pathways, the $q\Delta S(q, t)$ curves at early time delays (100 ps, 300 ps, and 1 ns) were fitted to a series of candidate pathways using the global fitting. The theoretical diffraction curves for each reaction pathway (Fig. 1) were based on density functional theory-optimized geometries and relative energies (Table 1). Because three-body dissociation is energetically impossible with one-photon excitation at 267 nm (448.2 kJ/mol), it is of interest to see whether our analysis can exclude this channel. Fig. 5 shows the comparison between $q\Delta S(q, t)$ at 100 ps and the corresponding fit results for various trial pathways. The residuals between the experimental data and the fits along with χ^2_{total} values are displayed for each pathway. The poor agreement between experiment and theory for the isomer channel precludes this pathway. The fit for the $HgI_2 \rightarrow HgI + I$ channel perfectly matches the experimental data over the whole q range as compared with other reaction channels. The fits for $HgI_2 \rightarrow Hg + 2I$ and $HgI_2 \rightarrow Hg + I_2$ in the high q region have a rather good figure of merit, but the fit is less good than the two-body dissociation channel. In fact, the $q\Delta S(q)$ curves from the solute-only contributions show very small differences at high q (25). In the fits for these channels, the residuals are more significant around the positive peak near 2 $Å^{-1}$ and around the negative peak at 3 $Å^{-1}$ than the fit for $HgI_2 \rightarrow HgI + I$ channel. In Fig. 4*A*, one can see that the contribution from the solvent to these peaks is not negligible. Thus, the apparent disagreements of the peak at 2 and 3 $Å^{-1}$ for $HgI_2 \rightarrow Hg + I + I$ and $HgI_2 \rightarrow Hg + I_2$ channels indicate that the solvent contribution in these channels is inconsistent with the associated transfer of energy to the solvent. These results establish that the $HgI_2 \rightarrow HgI + I$ reaction is the dominant pathway at 100 ps after 267-nm photodissociation of HgI_2 in methanol and that the solvent contribution helps to discriminate between candidate channels when the energetics is included. More importantly, when a mixture of $HgI_2 \rightarrow HgI + I$, $HgI_2 \rightarrow Hg + 2I$, and $HgI_2 \rightarrow Hg + I_2$ was fitted together against the $q\Delta S(q, t)$, the contributions of $HgI_2 \rightarrow Hg + I + I$ and $HgI_2 \rightarrow Hg + I_2$ converged to zero. We also considered the contribution of parent molecule with bent geometry from previous studies (30), which deteriorated the fits because the distance between I atoms in the bent structure (≈5.00 Å) is slightly smaller than in the linear geometry (≈5.30 Å). This finding illustrates the structural sensitivity of the TRXD data.

Conclusion

The results presented here clearly demonstrate the achievements of TRXD in determining concurrently the structure of excited solutes in their cages and the structure of the bulk solvent. By considering contributions from the solute, the solute–solvent cage, and the solvent response, we are able to generate theoretical difference–diffraction curves and fit them to the experimental diffraction patterns globally. The global analysis of TRXD data over a wide time range, from 100 ps to 1 μs, allows us to determine the primary reaction pathway, the subsequent reaction channels (recombination of various products), and the hydrodynamics of the solvent. Time-resolved liquid diffraction can, despite of the limited order in the liquid, reveal reaction kinetics of rather complex nature and involving several transient species.

Materials and Methods

Time-resolved diffraction data were acquired on the beamline ID09B at the European Synchrotron Radiation Facility (ESRF) using pump-probe technique (31). In brief, femtosecond laser pulses from a Ti:Sapphire laser, synchronized to single pulses of x-rays, were frequency tripled to 267 nm and temporally stretched to 2 ps by the passage through fused silica to prevent multiphoton excitation. The time-delayed x-ray pulses were selected from the 16-bunch filling mode of the synchrotron ring by using a synchronized mechanical chopper. Quasi-monochromatic 100-ps-long x-ray pulses with 5×10^8 photons per pulse were focused into in a 100×60 μm^2 spot at the sample. Diffraction data were collected with an area detector (MarCCD, Mar USA, Evanston, IL) with a sample-to-detector distance of 43 mm. A 10 mM solution of HgI_2 (Aldrich; 99.99%) in methanol was circulated through a high-pressure sapphire slit nozzle (0.3 mm thickness and ≈3 m/s jet speed). $\Delta S(q, t)$ values were generated by subtracting the reference data at −3 ns from the data at any other time delay (17).

Calculations for geometry optimization and energy minimization of the solute molecules and their presumed photoproducts in methanol environment were performed by B3PW91 (32) density functional theory as implemented in the GAUSSIAN 03 program (33). We used Polarizable-Continuum Model (PCM) (34) to describe the solvent effects. To include relativistic effect, we used Stuttgart relativistic large-core effective core potential for Hg atom (35). The intermolecular correlations of the related solute species with the solvent was obtained by MD simulation using the program MOLDY (36). The scattered intensity from each molecular configuration was calculated from the atom–atom distribution functions $g_{\alpha\beta}(r)$ by using our own programs and tabulated atomic formfactors. Detail descriptions of experimental and theoretical methods can be found in *Supporting Text*, which is published as supporting information on the PNAS web site.

We thank Rodolphe Vuilleumier, Savo Bratos, Philip Anfinrud, and Friedrich Schotte for their invaluable help with the theory and experiments. This work was supported by Korea Science and Engineering Foundation Nano R&D Program Grant 2005-02638 (to H.I.) and by European Union Grants HPRI-CT-1999-50004 and HPRN-CT-00160.

1. Ihee, H., Lorenc, M., Kim, T. K., Kong, Q. Y., Cammarata, M., Lee, J. H., Bratos, S. & Wulff, M. (2005) *Science* **309,** 1223–1227.
2. Lindenberg, A. M., Kang, I., Johnson, S. L., Missalla, T., Heimann, P. A., Chang, Z., Larsson, J., Bucksbaum, P. H., Kapteyn, H. C., Padmore, H. A., *et al.* (2000) *Phys. Rev. Lett.* **84,** 111–114.
3. Qulianov, D. A., Tomov, I. V., Dvornikov, A. S. & Rentzepis, P. M. (2002) *Proc. Natl. Acad. Sci. USA* **99,** 12556–12561.
4. Rose-Petruck, C., Jimenez, R., Guo, T., Cavalleri, A., Sider, C. W., Raksi, F., Siders, J. A., Walker, B. C., Wilson, K. R. & Barty, C. A. (1999) *Nature* **398,** 310–312.
5. Schotte, F., Lim, M., Jackson, T. A., Smirnov, A. V., Soman, J., Olson, J. S., Phillips, G. N., Wulff, M. & Anfinrud, P. A. (2003) *Science* **300,** 1944–1947.
6. Cao, J., Hao, Z., Park, H., Tao, C., Kau, D. & Blaszczyk, L. (2003) *Appl. Phys. Lett.* **83,** 1044–1046.
7. Ruan, C. Y., Vigliotti, F., Lobastov, V. A., Chen, S. & Zewail, A. H. (2004) *Proc. Natl. Acad. Sci. USA* **101,** 1123–1128.
8. Siwick, B. J., Dwyer, J. R., Jordan, R. E. & Miller, R. J. D. (2003) *Science* **302,** 1382–1385.
9. Srinivasan, R., Feenstra, J. S., Park, S. T., Xu, S. J. & Zewail, A. H. (2005) *Science* **307,** 558–563.
10. Bressler, C. & Chergui, M. (2004) *Chem. Rev.* **104,** 1781–1812.
11. Chen, L. X. (2005) *Annu. Rev. Phys. Chem.* **56,** 221–254.
12. Hargittai, I. (1988) *Stereochemical Applications of Gas-Phase Electron Diffraction, Part A: The Electron Diffraction Technique* (VCH, New York).
13. Pirenne, M. H. (1946) *The Diffraction of X-rays and Electrons by Free Molecules* (Cambridge Univ. Press, Cambridge, U.K.).
14. Harris, A. L., Brown, J. K. & Harris, C. B. (1988) *Annu. Rev. Phys. Chem.* **39,** 341–366.

15. Bratos, S., Mirloup, F., Vuilleumier, R., Wulff, M. & Plech, A. (2004) *Chem. Phys.* **304,** 245–251.
16. Cammarata, M., Lorenc, M., Kim, T. K., Lee, J. H., Kong, Q. Y., Pontecorvo, E., Lo Russo, M., Schiro, G., Cupane, A., Wulff, M., *et al.* (2006) *J. Chem. Phys.* **124,** 124504.
17. Plech, A., Wulff, M., Bratos, S., Mirloup, F., Vuilleumier, R., Schotte, F. & Anfinrud, P. A. (2004) *Phys. Rev. Lett.* **92,** 125505.
18. Wulff, M., Bratos, S., Plech, A., Vuilleumier, R., Mirloup, F., Lorenc, M., Kong, Q. Y. & Ihee, H. (2006) *J. Chem. Phys.* **124,** 034501.
19. Baumert, T., Pederson, S. & Zewail, A. H. (1993) *J. Phys. Chem.* **97,** 12447–12459.
20. Dantus, M., Bowman, R. M., Gruebele, M. & Zewail, A. H. (1989) *J. Chem. Phys.* **91,** 7437–7450.
21. Zhong, D. & Zewail, A. H. (1998) *J. Phys. Chem. A* **102,** 4031–4058.
22. Pugliano, N., Szarka, A. Z., Gnanakaran, S., Triechel, M. & Hochstrasser, R. M. (1995) *J. Chem. Phys.* **103,** 6498–6511.
23. Pugliano, N., Szarka, A. Z. & Hochstrasser, R. M. (1996) *J. Chem. Phys.* **104,** 5062–5079.
24. Volk, M., Gnanakaran, S., Gooding, E., Kholodenko, Y., Pugliano, N. & Hochstrasser, R. M. (1997) *J. Phys. Chem. A* **101,** 638–643.
25. Geis, A., Bouriau, M., Plech, A., Schotte, F., Techert, S., Trommsdroff, H. P., Wulff, M. & Block, D. (2001) *J. Luminescence* **94,** 493–498.
26. Somloi, J. & Tannor, D. J. (1995) *J. Phys. Chem.* **99,** 2552–2560.
27. Baskin, J. S. & Zewail, A. H. (1994) *J. Phys. Chem.* **98,** 3337–3351.
28. Aditya, S. & Willard, J. E. (1957) *J. Am. Chem. Soc.* **79,** 2680–2681.
29. Kwok, W. M., Ma, C. S., Parker, A. W., Phillips, D., Towrie, M., Matousek, P. & Phillips, D. L. (2000) *J. Chem. Phys.* **113,** 7471–7478.
30. Gaizer, F. & Johansson, G. (1968) *Acta Chem. Scand.* **22,** 3013–3016.
31. Wulff, M., Plech, A., Eybert, L., Randler, R., Schotte, F. & Anfinrud, P. A. (2003) *Faraday Discuss.* **122,** 13–26.
32. Becke, A. D. (1993) *J. Chem. Phys.* **98,** 5648–5652.
33. Frisch, M. J., Trucks, G. W., Schlegel, H. B., Scuseria, G. E., Robb, M. A., Cheeseman, J. R., Montgomery, J. A. J., Vreven, T., Kudin, K. N., Burant, J. C., *et al.* (2003) GAUSSIAN03 (Gaussian, Pittsburgh), Revision A. 1.
34. Cances, E., Mennucci, B. & Tomasi, J. (1997) *J. Chem. Phys.* **107,** 3032–3041.
35. Kuechle, W., Dolg, M., Stoll, H. & Preuss, H. (1991) *Mol. Phys.* **74,** 1245–1250.
36. Refson, K. (2000) *Comp. Phys. Comm.* **126,** 310–329.